IEEE Access
Multidisciplinary | Rapid Review | Open Access Journal

Received July 22, 2021, accepted September 14, 2021, date of publication September 20, 2021, date of current version September 29, 2021.

Digital Object Identifier 10.1109/ACCESS.2021.3114124

Sparse Multi-Channel Synthetic Aperture Radar Based Motion Induced Distortion Correction and Classification of Maritime Scenes

ROBERT W. JANSEN[1], (Member, IEEE), AND RAGHU G. RAJ[2], (Senior Member, IEEE)
[1]Remote Sensing Division, Naval Research Laboratory, Washington, DC 20375, USA
[2]Radar Division, Naval Research Laboratory, Washington, DC 20375, USA

Corresponding author: Robert W. Jansen (robert.jansen@nrl.navy.mil)

This work was supported by the Office of Naval Research through the U.S. Naval Research Laboratory 6.2 Base Program.

ABSTRACT Multi-channel Synthetic Aperture Radar (MSAR) in the maritime environment has proven to be an effective technique for improved image fidelity and scene characterization. Past demonstrations of MSAR-based methods for improvements such as motion induced distortion correction and image classification were performed using a uniformly spaced array of phase centers. In this paper, we derive novel extensions of these techniques to the case of sparse and non-uniformly spaced phase center configurations and demonstrate their effectiveness for a variety of platforms and sensor arrangements. We establish general techniques for correcting motion induced distortions, establish theoretical bounds of performance, and empirically validate our techniques on data derived from our airborne MSAR system. We then use these images to characterize the structure of the maritime scene using our MSAR-based classification technique. Our imaging and classification techniques are amenable to efficient implementation on diverse hardware platforms and sensor arrangements, and thus can find ready application in practical multichannel radar systems.

INDEX TERMS Multi-channel synthetic aperture radar (SAR), ocean imaging, image classification.

I. INTRODUCTION

Many applications in modern remote sensing and surveillance have tended towards the use of multiple sensors to probe the environment. Advancements in hardware miniaturization, computational power and storage have greatly contributed to the feasibility of various multi-sensor architectures—both collocated [10] and distributed varieties [11]. Such multi-sensor architectures can exploit various kinds of diversities in measurement—including spatial, temporal, and frequency—which lend robustness to inference operations performed on the sensed data. Multi-sensor architectures have the added benefit of lending agility to the operation of the overall system due to redundancies inherent in the system.

In the context of SAR imaging, there are a great variety of multichannel synthetic aperture radar (MSAR) sensor configurations and associated applications that have been shown over the past several years to be successful in delivering high-quality imaging products and higher swath coverage and more. However, here we are focused on a particular multi-sensor architecture that has been demonstrated to be well suited to highly-dynamic maritime imaging scenarios [1]–[5], [12], [13]. Specifically, MSAR systems have been shown to be very effective in combating blurring artifacts due to scene motion [1]–[4] and, more recently, for yielding superior classification performance in maritime sensing scenarios where the motion itself is a characteristic of different classes in the scene [5].

A fundamental problem in SAR imaging is the presence of distortions and smearing in the formed imagery due to the inherent ambiguity between stationary and moving scatterers present in the scene [1]. Consider a scatterer at range R from the sensing platform such that platform has a velocity of V_p (along the cross-range axis), and scatterer has a velocity of V_r (along the range axis). Then the Doppler shift associated with the scatterer is given by the well-known relationship [6]:

$$\delta_a = R * V_r / V_p \tag{1}$$

Thus the motions associated with a scatterer results in a spatial spreading and shifting of the target signature within

The associate editor coordinating the review of this manuscript and approving it for publication was Gerardo Di Martino.

the image. There are many different single-sensor based methods for compensating Doppler shifts associated with scatterer motion during the imaging process. These include: i) SAR-MTI methods based on analysis of the Doppler rate maps obtained from the range compressed raw data [7]; ii) Time-frequency based matching pursuit analysis of fluctuating scatterers in processed SAR images [8]; iii) Scatterer velocity estimation from the smear length of the scatterer (for the case when scatterer motion is only along azimuth direction) [6]; iv) Scatterer velocity estimation directly from a time-frequency analysis of chirp center frequency and chirp rates [6]. However all these methods suffer from a key limitation of ambiguities between stationary and moving returned signal histories and of being highly dependent on the SNR associated with the point scatterers. Thus they cannot be reliably and uniformly applied to the entire scene. These effects are especially exacerbated in maritime scenarios where virtually every scatterer is moving.

A much more elegant and powerful approach of combating the deleterious effects of scene motion is to add additional antenna receive elements to the moving platform aligned along the flight direction; this constitutes the aforementioned MSAR architecture [1]–[5]. There are 2 classes of processing structures that have proven to be successful for correcting these distortions using MSAR systems: 1) Fast Fourier Transform (FFT) based velocity SAR (VSAR) processing [9], [1]–[4] and 2) Multiple Along Track Interferometry (MATI) processing approach that was introduced in [1]. For the case of uniformly spaced arrays, both these methods have been shown to be roughly equivalent, modulo tradeoffs, in terms of overall imaging performance. These distortion corrected images can then be used as a starting point for further image analysis. In particular, on the side of classification, we have recently shown [5] that MSAR based systems furnish valuable covariance based motion information that complements traditional spatial amplitude based features, resulting in an elegant and superior approach to maritime scene classification [5].

This paper seeks to establish a natural generalization of MSAR digital processing algorithms to the case of sparse non-uniform arrays. The need for sparse non-uniform arrays arises in many applications where: i) all the available channels cannot be used due to high throughput requirements in real-time processing; ii) when a large enough baseline is desired in order to capture slow movers in the scene but where physical or design constraints force one to place the (sparse number of) antenna elements in non-uniformly spaced locations in the platform; or finally iii) when there are variations in signal quality across the channel that may preclude all the channels from being used. It also extends to satellite based systems where configurations of sensors may be highly variable or sparse.

We derive two classes of algorithms for the purpose of image distortion correction, the first involving the application of non-uniform DFT/FFT [16]–[18] and the second involving the application of M-ATI [1] methodology to non-uniform arrays. We derive theoretical limits of our algorithms and empirically validate their effectiveness on data captured by the U.S. Naval Research Laboratory (NRL) airborne MSAR system [3].

The rest of the paper is organized as follows. Section II establishes the MSAR system model for non-uniformed spaced sparse arrays. Section III introduces the NUDFT/FFT and MATI based imaging algorithms for sparse MSAR arrays together with a rigorous theoretical analysis of the bounds of velocity estimation in MSAR imaging systems. Thereafter, we empirically validate the novel sparse MSAR based image distortion correction algorithms.

In Section IV we describe our MSAR based classification algorithm that incorporates motion based structure derived from the MSAR array. Characterization of scene structure is accomplished by the application of our motion-based classification algorithm as demonstrated in Section V. We conclude the paper in Section VI with a discussion of directions for future research stemming from this work.

II. SPARSE MSAR SYSTEM MODEL

Consider a conceptual multichannel radar system consisting of M phase-centers that are non-uniformly spaced along a linear array with distances $\{\mathrm{d_m}\}_{m=1}^{M}$ from the first element of the array. We assume that array elements can arranged as follows: $\mathrm{d_m} = l_m\Delta$ for some $l_m \in \mathbb{Z}$ and $\Delta \in \mathbb{R}$; i.e. that the elements of the phased-array can be thought to be sub-sampled from a larger uniform linear array with element-separation of Δ. We define the largest possible such $\Delta = \Delta_p$ be the physical mesh-size of the non-uniform array.

The aforementioned non-uniform array can consist of a variety of different transmitting and receiving antennas combinations (including monostatic phase-centers that act as both transmitters and a receivers). All such configurations are equivalent, under suitable conditions of practical import, to having an array of virtual monostatic (i.e. transmit/receive) phase-centers whose positions lie half-way between the physical transmitter-receiver pair [14], [15]. It can be easily shown this mapping (to virtual phase centers) results in an equivalent non-uniform array with a virtual mesh-size, Δ_v, equal to one-half of the physical mesh-size, Δ_p, of the array. Fig. 1 illustrates the concept of virtual arrays in more detail—wherein we show three different configurations spanning: i) Configuration A: Uniformly spaced arrays, ii) Configuration B: Mildly non-uniformly spaced arrays and iii) Configuration C: Severely non-uniformly spaced array.

For the case of an airborne platform, such as the NRL MSAR system [3], a broadside-looking geometry is assumed and where the aircraft is assumed to be traveling along a straight line path with speed v and at a constant height above the ground plane. Let $I(z; m)$ be a complex SAR image formed from the I/Q (In-phase/Quadrature-phase) data collected from the m^{th} phase-center; where $z = (x, y)$ denotes the pixel position in the SAR image. We note that the index m varies over the non-uniform array indexed with respect to virtual array mesh-size Δ_v.

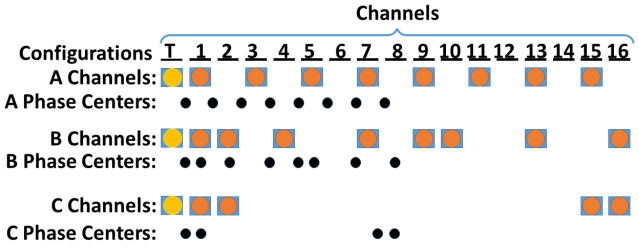

FIGURE 1. Physical vs. virtual array illustration: Different MSAR non-uniform array configurations sub-sampled from the NRL MSAR system.

The SAR image stack obtained in $\{I(z;m)\}_{m=1}^{M}$ forms the basis of MSAR processing. As mentioned in Section I, VSAR and M-ATI are two classes of processing structures that have proven to be successful for MSAR systems. The success of either of these operations, however, is predicated on correctly estimating the instantaneous phase information associated with each pixel of the image across the different phase centers. A perfectly stationary target should induce a constant phase across the different channels. In reality however, hardware imperfections can severely distort the amplitude and phase relationships between the different phase centers. To remove such channel to channel discrepancies, it is imperative to perform a channel balance step across the image stack prior to performing either the VSAR or MATI based processing steps. A channel balancing process has been successfully demonstrated in past literature [1], [15]. In particular, we employ the channel balancing approach described in [1] in our sparse MSAR based imaging algorithms.

Conditioned on the aforementioned channel balancing operation, the VSAR processing step involves performing a Fourier transform through the stack of SAR images across the phase centers, indexed by m, for each pixel in the image. This operation is captured by the following equation:

$$\mathbb{I}(z;k) = \sum_{m=1}^{M} w(m) I(z;m)\, e^{-jkm} \tag{2}$$

The power spectral density associated with $I_V(z;k)$ is given by:

$$P_V(z;k) = \left\langle \mathbb{I}(z;k), \mathbb{I}^*(z;k) \right\rangle \tag{3}$$

The link between VSAR and ATI based techniques comes from the concept of an interferogram between the SAR images produced by two different phase centers, m and m', which we define as follows [21], [22]:

$$\Gamma\left(z; m-m'\right) = \left\langle I(z;m), I\left(z;m'\right)\right\rangle \tag{4}$$

It can be easily shown that:

$$\mathcal{P}(z;k) \equiv \mathcal{F}_M\{I\} = \sum_{d=1}^{M-1} w_a(d)\Gamma(z;d)\, e^{-jkd} \tag{5}$$

such that: $\mathcal{F}_M$ is the $M-$ point FFT operator; d indexes the separation between the scatterers; and $w_a(d) = w(d) * w(-d)$ (where $*$ denotes the convolution operator).

In the next section we introduce MSAR based image analysis and classification algorithms in detail followed by a theoretical analysis of the velocity estimation properties of these algorithms in Section IV.

An MSAR system collects detailed backscattered information from a variety of multichannel geometries such as shown in Fig. 1. What is the best way to exploit this data in order to extract the underlying image information which includes fundamental operations such as focusing of scatterers, disambiguating scatterer positions arising from motion induced distortions artifacts, and ultimately, in the classification of higher-level scene structure? Fig. 2 shows a flow diagram of one such algorithmic design that successfully achieves these objectives in a computationally efficient manner that is amenable to real-time processing. The details of the various blocks in Fig. 2 are described throughout the paper. In this section we describe our methodology in detail; while the next section delves into the theoretical underpinnings of the optimality criteria associated with our algorithm.

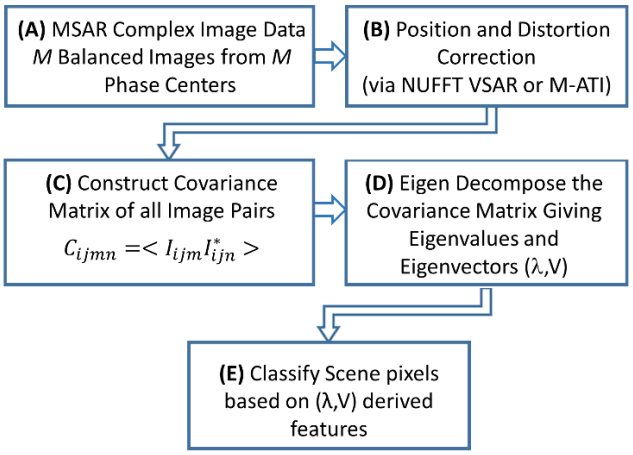

FIGURE 2. Summary of our MSAR based imaging and classification algorithm. (B) is detailed in Section III and (C)-(D) are described in Section IV of this paper.

III. SPARSE MSAR MOTION INDUCED DISTORTION CORRECTION

The first step of our algorithm involves the formation of images from the M phase centers of the MSAR system. In our paper we utilize the standard Chirp-Scaling algorithm [19] since it is computationally efficient when applied to large-scale images of practical interest. More generally any SAR imaging algorithm such as range-Doppler [19] or the fundamental backprojection algorithm [20] can be applied to obtain results similar to those reported in this paper. This step results, as described in Section I, in a stack of SAR images $\{I(z;m)\}_{m=1}^{M}$, corresponding to each phase-center m. In this paper we consider the general case where the phase-centers can be non-uniformly located. Subsections III-A and III-B below describe two novel algorithms for solving the fundamental issue of motion induced distortion correction. A theoretical analysis of the performance of the algorithms introduced in subsections III-A and III-B is presented in subsection III-C, while the experimental performance of

these algorithms, in terms of their ability to correct for motion-induced distortion, for non-uniform system architectures is demonstrated in subsection III-D.

A. NON-UNIFORM FFT BASED VELOCITY SAR ALGORITHM

The velocity SAR (VSAR) algorithm is a well-known technique in MSAR processing that has been applied for uniformly spaced along-track arrays. VSAR involves, as explained in Section II, performing a Fourier transform through the stack of SAR images across the phase centers, indexed by m, for each pixel in the image as given by equation (2) to yield an image stack $\{\mathbb{I}(z;k)\}_{k=1}^{M}$. Since the FFT operation effectively calculates the velocity spectrum associated with the pixel being examined, the motion induced distortion associated with the pixel can be removed simply by spatially shifting the scatterers by an extent determined by the velocity bin corresponding to the scatterer as per the equation:

$$\mathbb{I}^{s}(z;k) = \mathbb{I}(z + k\Delta_x; k) \tag{6}$$

where: $\Delta_x = \frac{R_0 \lambda P}{2V_p TN}$ is the effective pixel size [9] associated with the SAR image, P is the number of pulses, T is the time of integration, and N is the number of pixels associated with the azimuth length.

For the case of non-uniform arrays we propose a simple extension of (2) by performing instead a Non-Uniform Discrete Fourier Transform (NUDFT) operation along the image stack indexed by the phase centers, as follows:

$$\mathbb{I}_M^n(z;k) \equiv \mathcal{F}_{M,\xi_d}\{I\} = \sum_{d=0}^{M-1} w_a(d) I(z;d)\, e^{-jk\xi_d} \tag{7}$$

where: $\mathcal{F}_{M,\xi_d}$ is a particular type of $M-$ point NUDFT operator [16], [17] of interest to us in this paper where we sample non-uniformly in the spatial domain but uniformly in the $k-$ space; $\xi_m \in \{l_p - l_{p-1}\}_{m=1}^{M} \subset \{m | 0 \le m \le L/\Delta_p\}$, such that L and Δ_p are, respectively, the physical length and mesh size associated with the array; and $\{l_m\}_{m=1}^{M}$ are the locations of the M elements in the non-uniform array. We note that $\mathcal{F}_{M,\xi_d}$ reduces to standard FFT operator $\mathcal{F}_M$ for the case where the spatial sampling grid ξ_d is uniform. In the context of MSAR processing, focusing on the case of uniformly sampled k- field allows us to apply the standard VSAR based compensation methodology in equation (3) in order to remove motion induced distortion from the composite VSAR image.

The NUDFT based VSAR methods described above provides a method for obtaining the radial velocity spectrum automatically from first principles at every pixel in the image. The velocity resolution in this VSAR approach is inversely proportional to the number of channels M. Furthermore, this method retains the full image resolution available for the entire collection duration and utilizes the complete spectral information when determining the motion induced distortion correction to be performed at each pixel in the image. Finally the NUDFT operator can be effectively implemented via the Non-Uniform Fast Fourier Transform (NUFFT) algorithm while retaining all the benefits described above.

B. MULTI-CHANNEL ALONG TRACK INTERFEROMETRY (MATI)

This class of MSAR based motion distortion algorithm, introduced in [1], leverages insights from Along Track Interferometry (ATI) which is a commonly used method to determine speed of targets from a pair of azimuthally separated phase centers in SAR. For images $I(z;m_1)$ and $I(z;m_2)$ from phase centers m_1 and m_2 if we create the point-wise product:

$$I(z;m_1) * I^{*}(z;m_2) \;\; = Ae^{i\Delta\theta} \tag{8}$$

then the radial velocity field associated with pixel location z in the image is given by

$$V_r = \frac{\lambda_r V_p \Delta\theta}{4\pi d} \tag{9}$$

where λ_r is the radar wavelength, V_p is the platform speed and d is the spacing between phase centers. The separation d determines the upper bound of the velocity range available for non-ambiguous speeds due to 2π wrap around in $\Delta\theta$. On the lower velocity end, we need a value of d that will give sufficient phase difference $\Delta\theta$ to rise above noise.

Compared to the NUDFT-MSAR approach in section III-A, a severe limitation of (9) is that it samples a very limited portion of the velocity spectrum associated with the image and thus cannot be successfully applied to estimate the range of velocities distributed across the scene. To overcome this, we use a novel systematic method for measuring the full range of speeds within the limits of the full range of spacings by starting with the closest pairs (minimum d), mark pixels with phase differences above a noise threshold and then iterate the procedure for successive larger values of spacing d. This procedure reduces the possibility of phase wrap while achieving best available SNR by the use of multiple phase measurements (as available) at every velocity scale. Once we have determined the dominant velocity at every pixel we perform the shifts based on Eq. 1 to relocate targets to their proper locations. As a final step we fill in holes left by the shifted targets using sampling from surrounding pixels.

This method can be effectively used in multi-phase center system since we have a variety of phase-center separations d to choose from to compute speed. Thus for a given range of speeds we select pairs, as explained above, of phase-centers and calculate the sum:

$$V_r = \frac{1}{N} \sum_k \frac{\lambda_r V_p \Delta\theta}{4\pi d_k} \tag{10}$$

where: the summation in (10) is performed over all such phase-center pairs as described above.

We name the resulting algorithm multi-phase-center ATI (MATI) which has several important advantages over NUFFT-MSAR:

A1. Perhaps the biggest advantage of MATI is that, unlike NUFFT, there is no laborious interpolation operation involved regardless of configuration. The procedure to construct the velocity map works with whatever phase

center locations are available. Of course to get a continuous spectrum of velocities without phase wrap requires sufficient sampling of the along track space.

A2. The velocity measurements are continuous within a range. This is unlike VSAR where velocities are quantized in bins, which can lead to echo signatures if a target velocity spread spans two or more bins

A3. Finally MATI is in practice computationally much less effort than VSAR NUFFT-based methods.

The tradeoff is that MATI suffers from a clear drawback of not computing the full motion spectra at each pixel. This, however, is not a serious limitation in practice due to the fact that the spatial distribution of dominant velocities in a local patch is roughly equivalent to the VSAR-derived distribution of velocities. Furthermore, as the theoretical analyses and empirical results in the next two subsections show, the estimation of the velocities at each pixel using MATI is significantly improved due to the reduction in phase noise achieved by the averaging operation in (10).

C. THEORETICAL ANALYSIS

Our analysis focuses on the radar reflectivity and processing of a localized target motion patch for which we derive velocity resolution estimates via along-track interferometric (ATI) and Fourier spectral analysis performed on the non-uniform array. Consider the following model for radar spatial reflectivity of a localized target motion patch:

$$\mathcal{T}(z;t) = \sum_{k=1}^{K} a_k C_z exp\left(j\left(\frac{4\pi v_k t}{\lambda V_p} + \epsilon_k\right)\right) \times \delta\left(v^k - v_z\right) n(z,t) \quad (11)$$

where: $z = (x, y)$ is the spatial coordinate associated with the localized motion patch $\mathcal{T}$; K is the number of scatterers in the motion patch $\mathcal{T}$; a_k is the scattering amplitude of the k^{th} scatterer; v_z is a random variable associated with the velocity profile corresponding to z to which we ascribe a discrete measure that maps a set of scatterer velocities $\{v_k\}_{k=1}^{K}$; $\epsilon_k = \mathcal{N}(0, \sigma_\epsilon)$ is the phase-noise associated with the k^{th} scatterer; $C_z = exp\left(\frac{-\pi z_1^2}{W_x^2}\right) exp\left(\frac{-\pi z_2^2}{W_y^2}\right)$ such that W_x and W_y are the characteristic dimensions of $\mathcal{T}$; and where n is a zero-mean Gaussian random process with covariance:

$$\left\langle n(z,t),\ n^*\left(z',t'\right)\right\rangle = \delta\left(z_1 - z_1'\right)\delta\left(z_2 - z_2'\right) \times \exp\left(-\frac{\left(t-t'\right)^2}{\tau_s}\right) \quad (12)$$

The model (11) reduces to commonly used models in the literature [9], [21], [22] for the special case where the local target patch consists of a dominant velocity component.

From our analysis in Appendix A1 we have that:

$$\mathcal{P}_{\mathcal{T}}(x,k) \equiv \mathcal{F}\{w_a \Gamma_{\mathcal{T}}\} = \sum_{d=1}^{M-1} w_a(d)\Gamma_{\mathcal{T}}(z;d)\, e^{-jkd} = \sum_{k=1}^{K} |b_k|^2 |C_z|^2 \tilde{W}_a\left(k - \frac{4\pi v_r^k}{\lambda V}\right) \quad (13)$$

where:

$$\tilde{W}_a = W_a * exp\left(-\tau_s k^2\right)$$

and

$$W_a(k) = \sum_{d=0}^{M-1} w_a(d) exp(-jkd)$$

The velocity spectrum uncovered by (13) demonstrates that the VSAR operator, unlike ATI, intrinsically facilitates eliciting multiple velocity components $\left\{v_r^k\right\}_{k=1}^{K}$ present in $\mathcal{T}$. We experimentally demonstrate this in Section IV.

Thus far we have confined our spectral analysis to the case of uniformly sampled arrays. More generally we consider the case where spectral analysis in (13) is performed over a non-uniformly sampled array:

$$\mathcal{P}_{\mathcal{T}}(x,k) \equiv \mathcal{F}_{M,\xi_d}\{w_a \Gamma_{\mathcal{T}}\} = \sum_{d=0}^{M-1} w_a(d)\Gamma_{\mathcal{T}}(z;d)\, e^{-jk\xi_d} \quad (14)$$

Since the NUDFT operator $\mathcal{F}_{M,\xi_d}$ performs non-uniform sampling in the spatial domain and uniformly in the $k-$space, this in turn allows us to apply the standard VSAR based compensation methodology [9] to the resulting power spectrum (14).

Interpreting $\mathcal{F}_{M,\xi_d}$ as a matrix operator, where $\left[\mathcal{F}_{M,\xi_d}\right]_{kd} = e^{-2\pi jk\xi_d/M}/\sqrt{M}$, consider evaluating the function $f(\xi) = \sum_{d=0}^{M-1} b_d e^{2\pi jd\xi}$ at M distinct points $0 \le l_0 \le l_1 \le \cdots \le l_{M-1} < 1$ yields the matrix equation $f = \mathcal{F}_M^n b$, where $b = [b]_l \in \mathbb{C}^M$. In general $\mathcal{F}_M^n$ is a frame operator [23] whose columns are in general linearly dependent and yet span the space $\mathbb{C}^M$. We consider therefore the set of all functions spanned by frame elements of $\mathcal{F}_M^n$ as:

$$\mathfrak{T}_N = \left\{f(\xi) = \sum_{m=-M}^{M} b_j e^{j2\pi m\xi};\ b_{-N}, \ldots, b_N \in \mathbb{C}\right\}$$

An important measure the ability of the NUDFT based VSAR system to resolve scatterer velocities hinges on the resolution of the power spectrum which in turn depends on the invertibility of the frame operator $\mathcal{F}_{M,\xi_d}$. The following theorem, which is based on frame theoretic ideas [23], [24] and proved in Appendix A2, makes this relationship more precise.

Theorem 1 (NUDFT-VSAR): Let $\{l_i\}_{i=0}^{M-1}$ be the locations of the phase-centers of a non-linear VSAR system such that: $0 \le l_0 \le l_1 \le \ldots \le l_{M-1} < 1$. Let $\delta = \max_{0 \le i \le M-1} (l_{i+1} - l_i)$ and $v_i = (l_{i+1} - l_{i-1})/2$. Suppose $N \in \mathbb{Z}$ is defined such that $\delta < 1/(2N)$; then, let $D_N(\xi) = sin((2N+1)\pi\xi)/sin(\pi\xi)$ be the Dirichlet kernel. Then the collection $\left\{\sqrt{v_i} D_N(. - l_i)\right\}_{i=0}^{M-1}$ is a frame for the space $\mathfrak{T}_N$ with lower frame bound $A = (1 - 2\delta N)^2$ and upper frame bound $B = (1 + 2\delta N)^2$. □

Remarks:

R1. The condition $\delta < 1/(2N)$ enforces the fact that $M > 2N$. For the case of the uniformly spaced array we have that $l_i = i/M$ whereby if $M = 2N+1$ then the collection $\{D_N(. - i/M)\}_{i=0}^{M-1}$ is an orthonormal basis for $\mathfrak{T}_N$.

R2. For the case of uniformly spaced arrays, $\delta = 1/M$ since $l_i = i/M$ for all i, and consequently the power spectrum exhibits unique signatures corresponding to each scatterer velocity present in the localized target motion patch $\mathcal{T}$

R3. For the case of a non-uniform array, the condition $\delta < 1/(2N)$ guarantees a stable reconstruction of the signal.

R4. Theorem 1 does not give any guarantees for highly non-uniform cases where, as the experimental results show in the next section, NUFFT based approach does not effectively remove motion based distortions. However alternative methods can be employed for the case where there is structure in the signal. In particular when any given location in the scene has only a few dominant motion components then methods such as Sparse FFT [25], Prony based estimation [26] and other spectrum estimation methods can be employed. As discussed above, in this paper we use an ATI based approach for this case which demonstrates superior performance under highly non-uniform sampling conditions. In particular, Theorem 2 below shows how our MATI algorithm can correctly estimate the scatterer velocities in the given region under suitable regularity conditions

Definition (MATI operator): For an image patch $\mathcal{T}(z;t)$ we define the MATI operator $\mathcal{M}(\mathcal{T})$ as follows:

$$\mathcal{M}(\mathcal{T}) = \frac{1}{M}\sum_{m=1}^{M_z} \frac{\lambda v_p}{4\pi d_m} \sphericalangle \left\langle \mathcal{T}\left(z; l_{\mathcal{J}_z(m)}\right), \mathcal{T}\left(z; l_{\mathcal{J}_z(m-1)}\right)\right\rangle \tag{15}$$

where: $M_z \equiv$ number of phase center pairs (from smallest to highest separation); $\mathcal{J}_z \equiv$ index set corresponding to location z; $d_m = l_m - l_{m-1}$, $\sphericalangle$ and $\langle , \rangle$ are, respectively, the phase and inner product operators. □

The following Theorem, proved in Appendix 2, shows how the MATI operator correctly estimates the velocity field under suitable regularity conditions on the velocity field corresponding to image patch $\mathcal{T}$.

Theorem 2 (MATI): Let v_z be a Gaussian Random Field with velocity spectrum $S(\omega_v)$. Then we have that:

$$\mathbb{E}_{v_z}\left[\|\mathcal{M}(\mathcal{T}) - v_z\|_2\right] \leq \frac{\lambda v_p}{4\pi d_m}\frac{1}{M}\int S(\omega_v)\, d\omega_v \tag{16}$$

where: $M \equiv$ number of ATI phase centers over which the averaging operation is performed in $\mathcal{M}(\mathcal{T})$. □

Though the NUDFT-VSAR approach performs a much more detailed analysis of the velocity spectrum at each location in the image patch, Theorem 2 indicates that the velocity at each such location can nevertheless be accurately estimated by exploiting the spectral regularity of the velocity distribution in the region of interest via the averaging operation in (10).

The above analysis demonstrates relative trade-offs between ATI and Fourier based analyses of the velocity spectra inferred from MSAR systems. The next section describes the empirical performance of MSAR based motion distortion algorithms in greater detail.

D. EMPIRICAL PERFORMANCE OF MSAR MOTION DISTORTION ALGORITHMS

Fig. 3 shows the empirical performance of both the NUFFT-VSAR and MATI based MSAR motion induced distortion correction algorithms when applied to data captured by the NRL airborne MSAR system. The collection was performed in the Oregon Inlet, North Carolina, USA region in the Fall of 2015. Fig. 3(a) show the original SAR image captured without distortion correction. We note that both the boats present in the scene have been significantly displaced from the correct location due to Doppler shifts associated with the scatterer as given by (1). This underlying mechanism also contributes to defocusing of the scene due to motion induced distortions.

For the case of uniformly spaced arrays (i.e. Configuration A in Fig. 1), Configuration A in Figs. 3(b) and 3(c) show, respectively, the results of NUFFT-VSAR and MATI distortion correction algorithms. It is clear that NUFFT-VSAR algorithm renders superior distortion correction results; for example, we observe that the boats are repositioned to their correct location and that the smearing associated with the motion of the boat has been compensated much better than MATI is able to achieve. Likewise better focusing is achieved throughout the image due to NUFFT-based VSAR processing.

We next consider the mildly non-uniform case depicted in Configuration B in Fig. 3. The performance of NUFFT-VSAR and MATI distortion correction algorithms, respectively, are shown in Figs. 3(d) and 3(e) (corresponding to Configuration B). Once again we observe that NUFFT- VSAR performs comparatively better than MATI both in terms of correctly placing the movers and correcting the overall motion induced distortion in the scene.

For both the above cases, the superior performance of NUDFT-VSAR is because VSAR performs a much more detailed analysis of the velocity spectrum at each location corresponding to the image patch together with the fact that the sufficient conditions of Theorem 1 are met.

However for the highly non-uniform case, corresponding to Configuration C, we find that NUFFT-VSAR performed poorly relative to MATI since the conditions of Theorem 1 are no longer met. Nevertheless MATI continues to demonstrate reasonable performance due to exploiting regularity conditions of the scene as indicated by Theorem 2. The echoes, corresponding to the boat, that appear in Fig. 3(g), are due to phase unwrapping issues which are in general difficult to compute in practice. The MATI algorithm however is far less dependent on such phase unwrapping due to the phase-center pair selection procedure that we use as described above.

IV. MSAR BASED CLASSIFICATION ENGINE

Once the motion induced distortions have been corrected by employing the methods described in section III,

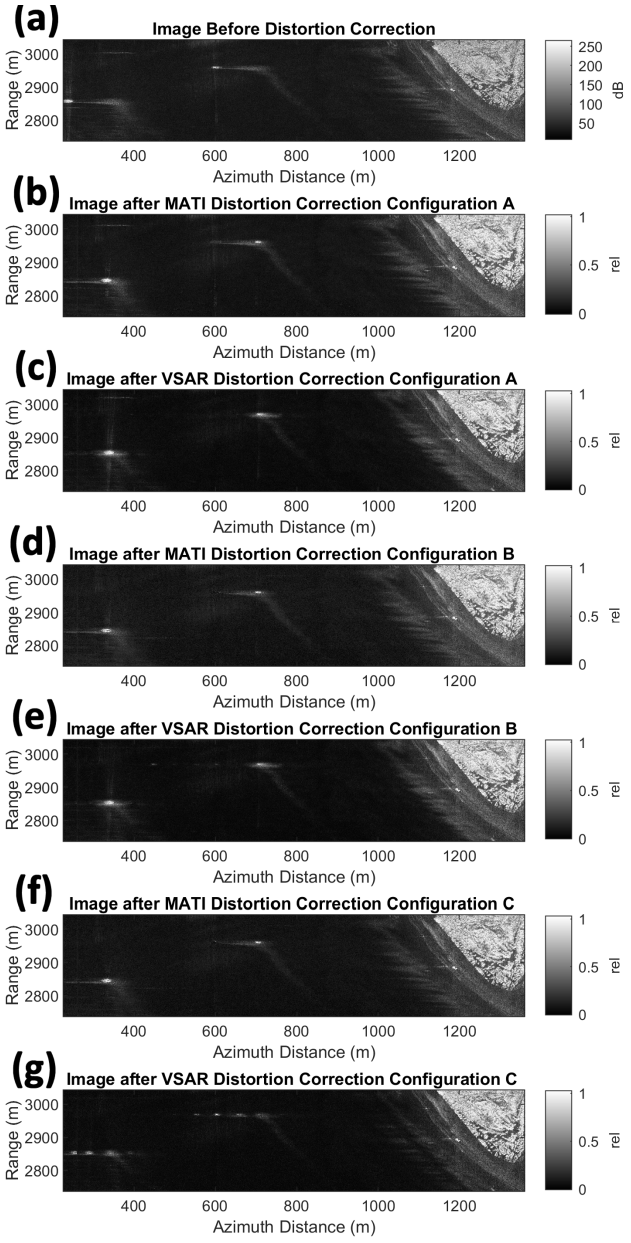

FIGURE 3. Empirical performance of NUFFT-VSAR and MATI based MSAR motion induced distortion correction algorithms (the data collection was performed in the oregon inlet, north carolina, USA region in the Fall of 2015.). Though NUFFT-VSAR is more suitable for uniform or nearly uniform placement of phase-centers, MATI is much more robust and easier to implement for highly non-uniform settings.

the higher-level information about scene structure can be obtained by applying a suitable classification engine. In our previous work we have designed a novel classification engine that is well suited to exploiting the motion based features inherent in the MSAR system—and in a way that complements traditional amplitude based approaches to image classification. An important ingredient of our method is to capture motion information at each pixel, (i, j). We start by constructing the covariance array for all phase-center pairs (m, n):

$$C_{ijmn} = < I_{ijm} I^*_{ijn} > . \tag{17}$$

The spatial averaging implied in (17) is over a window smaller than the smallest targets of interest. At each pixel, (i, j) we generate the M eigenvalues λ_m and eigenvectors $\vec{v_m}$ ($m = 1$ to M) of the covariance matrix $\boldsymbol{C}$

$$\boldsymbol{C}\ \vec{v_m} = \lambda_m \vec{v_m} \tag{18}$$

for use in our classification procedure. We drop the (i, j) indices for brevity. The eigenvalues and eigenvectors characterize the in-scene motions at each pixel throughout the MSAR collection time.

For a pixel containing a coherent, dominant scatterer, the MSAR image stack will be proportional to

$$S \propto \left[1,\ e^{i\Delta\phi},\ e^{i2\Delta\phi},\ e^{i3\Delta\phi}, \ldots ,\ e^{i(M-1)\Delta\phi}\right]$$

using M images, and the resulting covariance matrix is then

$$C = S^{\dagger}.S \propto \begin{bmatrix} 1 & e^{i\Delta\phi} & \cdots & e^{i(M-1)\Delta\phi} \\ e^{-i\Delta\phi} & 1 & & \vdots \\ \vdots & & \ddots & \\ e^{-i(M-1)\Delta\phi} & \cdots & & 1 \end{bmatrix} \tag{19}$$

where $S^{\dagger}$ is the Hermitian conjugate of S. Eigen analysis of this covariance matrix identifies a single large eigenvalue and its associated eigenvector. Further details of the eigen-analysis of (23) and its relationship to dominant scattering mechanisms is given in [5].

Given this, the key idea is to perform an eigen-analysis of the multichannel covariance matrix associated with each scatterer in the image. The explicit form of the boxcar averaged covariance matrices that we employ is given by:

$$C^{i,j}_{m,n} = \sum_{k=-\Delta_x}^{\Delta_x} \sum_{l=-\Delta_y}^{\Delta_y} C_{i-k,j-l;m,n} \tag{20}$$

where Δ_x, Δ_y are the local spatial windows along the respective image axes, and $C_{i-k,j-k;mn}$ are the rank-1 covariance matrix from (17). The calculation in (20) serves the two-fold purpose of reducing image speckle and increasing the rank of the covariance matrix, $C^{i,j}_{m,n}$, by aggregating motion information in a localized neighborhood of each pixel. The resulting eigenvalues and eigenvectors reveal valuable information relating to the signature motion characteristics of the classes of interest [5].

From the eigenvalues and eigenvectors extracted above, we calculate a set of features outlined in Fig. 4 (and explained in more detail in [5]) and applied a standard support vector machine (SVM) classification engine to classify each pixel into one of the following categories: Ambient, Surf, Boat, Wake, Land, and Beach. This completes the description of our general sparse MSAR based imaging and classification procedure shown in Fig. 2.

From our results in Section III-C, due to its more robust performance compared to NUFFT-MSAR on non-uniform arrays, we employ MATI as our algorithm of choice for sparse MSAR based motion distortion correction before applying the aforementioned classification algorithm. Section V describes the experimental results in detail.

Feature 1: Entropy

$$F_1 = -\sum_{m=1}^{M} \lambda_m \ln \lambda_m$$

Feature 2-4: Eigenvalue differences

$$F_{2,3,4} = (\lambda_m - \lambda_{m+1})/\lambda_1, \quad m = 1 \text{ to } 3$$

Feature 5, 6: Eigenvector coherence

$$F_{5,6} = \frac{\left|\sum_{k=1}^{M-1} v_{k,m}\, v^*_{k+1,m}\right|}{\sum_{k=1}^{M-1} \left|v_{k,m}\, v^*_{k+1,m}\right|}, \quad m = 1 \text{ to } 2$$

Feature 7, 8: Local eigenvalue

$$F_{7,8} = \sqrt{\frac{1}{n}\sum_{ij}^{n} (\lambda_{ij,m} - \bar{\lambda}_m)^2}, m = 1, 2$$

Feature 9, 10: Eigenvector phase slope

$$F_{9,10} = \left| \frac{\frac{1}{n(M-1)} \sum_{ij}^{n} \sum_{k=1}^{M-1} \Delta_{ij,k,m}}{\frac{1}{n(M-1)} \sqrt{\sum_{ij}^{n} \sum_{k=1}^{M-1} (\Delta_{ij,k,m} - S_m)^2}} \right|$$

where $\Delta_k = \phi_k - \phi_{k+1}$

$$S_m = \frac{1}{n(M-1)} \Sigma_{ij}^{n} \Sigma_{k=1}^{M-1} \Delta_{ij,k,m}$$

$m = 1, 2$

FIGURE 4. Summary of the covariance matrix eigenvalue and eigenvector v derived features employed in our MSAR based classification algorithm [5].

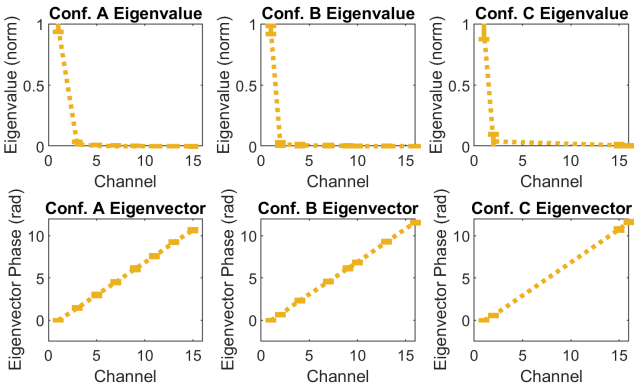

FIGURE 5. Eigen-based features associated with the boat after MATI-based distortion correction as shown in Figure 3.

V. EXPERIMENTAL RESULTS FOR SPARSE MSAR BASED CLASSIFICATION

The previous sections have both theoretically and empirically established the robustness of the MATI algorithm compared to NUDFT based approach to motion distortion correction. Given the robustness of the MATI algorithm for a wide range of non-uniform sampling patterns (as compared to the NUDFT-VSAR case), we focus only on MATI based scene distortion corrected images for the classification results in this paper.

Fig. 5 shows the eigenvalues and eigenvectors corresponding to the boat in Fig. 3, as estimated by the MATI algorithm. We find that our sparse MSAR classification procedure is remarkably robust to variations in the sampling configurations and that for even extremely non-uniform sampling cases, i.e. Configuration C, the estimation of the eigenfeatures compare remarkably well to the baseline uniform sampling case in Configuration A. In particular the estimation of the phase slope remains constant for all cases although Configuration C requires higher level phase unwrapping. We point out that such phase unwrapping is unnecessary in our MATI algorithm (unlike NUFFT-VSAR) because, as explained in Section III-B, we only chose a select set of phase-center pairs commensurate with the velocity range under consideration.

Fig. 6 demonstrates the classification performance of the sparse MSAR classification algorithm with MATI distortion corrected images for all non-uniform sampling cases ranging from uniform (Configuration A) to highly non-uniform (Configuration C). In all cases we find that our sparse MSAR based image classification approach yields extremely robust classification performance in that all of the component classes such as surf, beach etc. are largely correctly and consistently identified even in highly non-uniform sampling scenarios although all cases show some difficulty distinguishing wake vs surf as they both exhibit very similar signatures.

Finally Fig. 7 gives a quantitative performance of the classification rate of the sparse MSAR classification algorithm for the various classes comprising the scene. We observe that, except for the wake class, the drop in classification

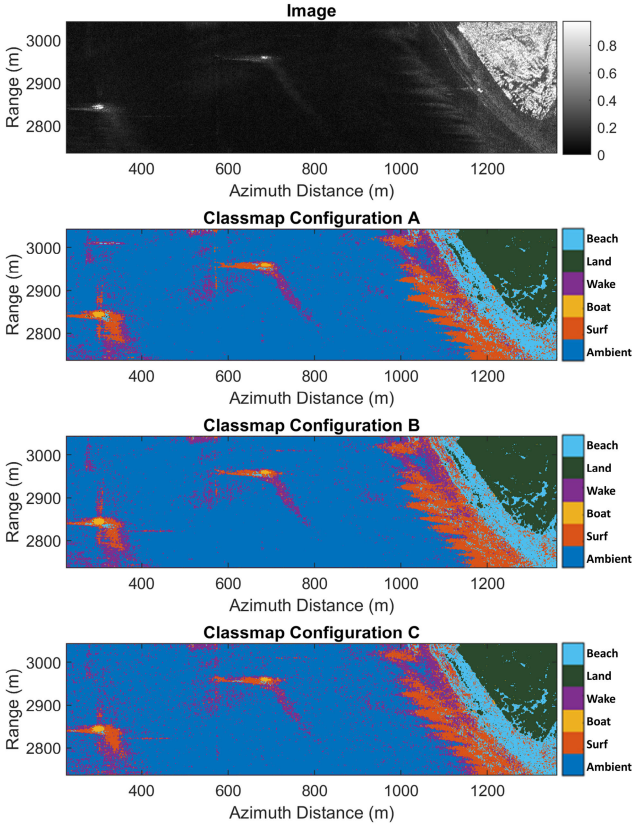

FIGURE 6. MSAR based image classification when applied to maritime scenes for three sparse sensor configurations.

performance in both mild (Configuration B) and highly (Configuration C) non-uniform sampling is very consistent with the uniform sampling case (Configuration A). The appreciable loss in performance for the case of the wake structure is likely due to the fact that the spatial regularity conditions in Theorem 2 do not hold whereby multiple dominant velocity components are present in every location of the scene. An open problem thus raised by our work is the formulation of robust estimators of complex motion structure of turbulent sources such as wakes.

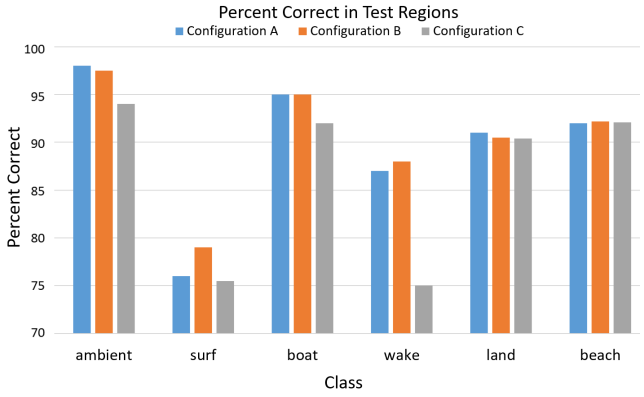

FIGURE 7. Quantitative MSAR based classification performance on maritime scene structures.

VI. CONCLUSION

This paper has established the first known generalization of previous works on MSAR based imaging and classification to the case of sparse, non-uniformly spaced arrays. The need for such sparse MSAR systems is important for various applications such as space-based and practical airborne applications where sensors generally are not arranged in a strictly uniform array due to one more practical constraints such as the requirements in real-time processing, the need to enforce a large enough baseline to capture slow movers under physical sensing constraints, and finally the need for sparse sensor selection conditions due to variations in signal quality across channels.

To this end, this paper has uncovered generalized processing structures—the NUFFT-VSAR and MATI algorithms—for performing motion distortion correction with applications to MSAR based maritime scene classification. We rigorously examined the theoretical and empirical properties of these techniques with regards to motion distortion and also demonstrated the remarkably robust performance of the MATI distortion correction and MSAR-based classification algorithm with respect to even highly non-uniform sampling scenarios. Our resulting sparse MSAR based imaging and classification algorithm optimally utilizes the sparse structure of the antenna array in a manner that is amenable to real-time processing. The imaging and classification techniques developed in this paper should thus find ready application on multi-channel SAR platforms thereby significantly broadening the impact of MSAR based methods in various remote sensing and surveillance applications.

Future work stemming from our work includes the formulation of robust estimators of complex motion structure of turbulent sources such as wakes, and the formalization of end-to-end MSAR classification structures via deep learning based processing architectures.

APPENDIX

A. APPENDIX A1

We spectrally analyze the reflectivity model in (15) using (4-5). By definition, $\Gamma_{\mathcal{T}}(z;d) = \langle \mathcal{T}(z;m+d), \mathcal{T}(z;m)\rangle$. Thus we have that:

$$\begin{aligned}
&\Gamma_{\mathcal{T}}(z;d) \\
&= \left\langle \sum_{k=1}^{K} b_k C_z exp\left(j\left(\frac{4\pi v_k (m+d)}{\lambda V_p} + \epsilon_k\right)\right)\right. \\
&\times \delta\left(v_z - v^k\right) n(z,(m+d)), \sum_{l=1}^{K} b_l C_z \\
&\left.\times exp\left(j\left(\frac{4\pi v_l m}{\lambda V_p} + \epsilon_l\right)\right)\delta\left(v_z - v^l\right) n(z,m)\right\rangle \qquad \text{(A1)} \\
&= \sum_{k=1}^{K}\sum_{l=1}^{K} b_k b_k^* |C_z|^2 exp\left(j\left(\frac{4\pi v_k (m+d)}{\lambda V_p} + \epsilon_k\right)\right) \\
&\times exp\left(-j\left(\frac{4\pi v_l m}{\lambda V_p} + \epsilon_l\right)\right)\delta\left(v_z - v^k\right) \\
&\times \delta\left(v_z - v^l\right)\langle n(z,(m+d)), n(z,m)\rangle \qquad \text{(A2)} \\
&= \sum_{l=1}^{K} |b_k|^2 |C_z|^2 exp\left(j\left(\frac{4\pi v_k d}{\lambda V_p}\right)\right) \\
&\times \langle n(z,(m+d)), n(z,m)\rangle \qquad \text{(A3)} \\
&= \sum_{k=1}^{K} |b_k|^2 |C_z|^2 exp\left(j\left(\frac{4\pi v_k d}{\lambda V_p}\right)\right) \\
&\times \delta(z_1 - z_1)\delta(z_2 - z_2) exp\left(\frac{-d^2}{\tau_s}\right) \qquad \text{(A4)} \\
&= \sum_{k=1}^{K} |b_k|^2 |C_z|^2 exp\left(j\left(\frac{4\pi v_k d}{\lambda V_p}\right)\right) exp\left(\frac{-d^2}{\tau_s}\right) \qquad \text{(A5)}
\end{aligned}$$

Then again by the definition of $\mathcal{P}_{\mathcal{T}}(x,k)$, we have:

$$\begin{aligned}
\mathcal{P}_{\mathcal{T}}(x,k) &= \sum_{d=0}^{M-1} w_a(d)\Gamma_{\mathcal{T}}(z;d)\, e^{-jkd} \\
&= \sum_{d=0}^{M-1} w_a(d)\left(\sum_{k=1}^{K} |b_k|^2 |C_z|^2\right. \\
&\left. exp\left(j\left(\frac{4\pi v_k d}{\lambda V_p}\right)\right) exp\left(\frac{-d^2}{\tau_s}\right)\right) e^{-jkd} \qquad \text{(A6)} \\
&= \sum_{k=1}^{K} |b_k|^2 |C_z|^2 \left(\sum_{m=0}^{M-1} w_a(d)\right. \\
&\left. exp\left(j\left(\frac{4\pi v_k d}{\lambda V_p}\right)\right) exp\left(\frac{-d^2}{\tau_s}\right) e^{-jkd}\right) \qquad \text{(A7)} \\
&= \sum_{k=1}^{K} |b_k|^2 |C_z|^2 \mathcal{F}\left(w_a(d) exp\left(j\left(\frac{4\pi v_k d}{\lambda V_p}\right)\right)\right. \\
&\left. exp\left(\frac{-d^2}{\tau_s}\right)\right) \qquad \text{(A8)} \\
&= \sum_{k=1}^{K} |b_k|^2 |C_z|^2 \tilde{W}_a\left(k - \frac{4\pi v_r^k}{\lambda V}\right) \qquad \text{(A9)}
\end{aligned}$$

where: $\tilde{W}_a = W_a * exp\left(-\tau_s k^2\right)$ and $W_a(k) = \sum_{d=0}^{M-1} w_a(d) exp(-jkd)$ □

B. APPENDIX A2

Here we show the proof of Theorem 1 in Section III-C

Proof (Theorem 1: NUDFT-VSAR): Let $\eta_i = (l_{i-1} + l_i)/2$ be the mid-point of the interval $[l_{i-1}, l_i]$. Our strategy is to

approximate the function $f \in \mathfrak{T}_N$ being modeled by a projection to the space of piece-wise constant functions via the operator $Q : \mathfrak{T}_N \to L^2[0, 1]$ as follows:

$$Qf = \sum_{i=0}^{M-1} f(l_i)\, \Pi_{[l_i,\, l_{i+1}]} \tag{A10}$$

where,

$$\Pi_{[l_i,\, l_{i+1}]}(x) = \begin{cases} 1 & x \in [l_i, l_{i+1}] \\ 0 & else \end{cases}$$

$$\Rightarrow \|Qf\|_2^2 = \sum_{i=0}^{M-1} v_i |f(l_i)|^2 \tag{A11}$$

Thus we have that:

$$\begin{aligned} &\|(f - Qf)(x)\|_2^2 \\ &= \sum_{i=0}^{M-1} \int_{\eta_i}^{\eta_{i+1}} |f(x) - f(l_i)|^2 .dx \qquad \text{(A12)} \\ &= \sum_{i=0}^{M-1} \left(\int_{\eta_i}^{l_i} |f(x) - f(l_i)|^2 .dx \right. \\ &\left. + \int_{l_i}^{\eta_{i+1}} |f(x) - f(l_i)|^2 .dx \right) \qquad \text{(A13)} \\ &\leq \sum_{i=0}^{M-1} \frac{4}{\pi^2} \left(\frac{\delta}{2}\right)^2 \int_{\eta_i}^{\eta_{i+1}} |f'(x)|^2 .dx \qquad \text{(A14)} \\ &\leq 4\delta^2 M^2 \|f\|_2^2 \qquad \text{(A15)} \end{aligned}$$

where: (A14) follows from Wirtinger's inequality [24] and (A15) follows from Bernstein's inequality [24].

Therefore:

$$\begin{aligned} \left\| (I - Q)|_{\mathfrak{T}_N} \right\| \;&\leq\; 2\delta M \;<\; 1 \\ &\Rightarrow\; \|f - Qf\| \leq 2\delta M \, \|f\| \\ &\Rightarrow\; |\|f\| - \|Qf\|| \leq 2\delta M \, \|f\| \end{aligned}$$

(by the opposite triangle inequality)

$$\begin{aligned} &\Rightarrow\; -2\delta M \, \|f\| \leq \|f\| - \|Qf\| \leq 2\delta M \, \|f\| \\ &\Rightarrow\; (1 - 2\delta M) \, \|f\|_2^2 \leq \|Qf\|_2^2 \leq (1 + 2\delta M) \, \|f\|_2^2 \end{aligned}$$

This completes the proof (given (*A6*) and since

$$\sum_{i=0}^{M-1} v_i |f(l_i)|^2 = \sum_{i=0}^{M-1} \left| \langle f, \sqrt{v_i} \rangle D_N(. - l_i) \right|^2)$$

□

C. APPENDIX A3

Here we show the proof of Theorem 2 in Section III-C

Proof (Theorem 2: MATI):

$$\begin{aligned} &\mathbb{E}_{v_z} \left[\|\mathcal{M}(\mathcal{T}) - v_z\|_2 \right] \\ &= \mathbb{E} \left[\|\mathcal{M}(\mathcal{T}) - v_z \mid v_z\|_2 \right] \\ &= \frac{1}{M} \sum_{m=1}^{M_z} \frac{\lambda v_p}{4\pi d_m} \mathbb{E} \\ &\quad \times \left[\sphericalangle \left\langle \mathcal{T}\left(z; l_{\mathcal{J}_z(m)}\right), \mathcal{T}\left(z; l_{\mathcal{J}_z(m-1)}\right) \right\rangle \mid v_z \right] \end{aligned}$$

(by definition of the MATI operator in (19))

$$\leq \mathbb{E} \left[\frac{1}{M} \left\| \sum_{m=1}^{M} \frac{\lambda v_p}{4\pi d_m} \left[\frac{4\pi d_m}{\lambda v_p} v_z + \epsilon_{k_z} \right] - v_z \right\|_2 \right]$$

(where: $k_z = \underset{k \in [1,\, 2, \ldots K]}{\operatorname{argmin}} \|v_k - v_z\|$)

$$= \mathbb{E} \left[\left\| \tilde{\epsilon}_{k_z} \right\|_2 \right]$$

(where: $\tilde{\epsilon}_{k_z} = \frac{\lambda v_p}{4\pi d_m} \frac{1}{M} \sum_{m=1}^{M} \epsilon_{k_z} \mathcal{N}\left(0, \frac{\lambda v_p}{4\pi d_m} \frac{1}{M} \int S(\omega_v)\, d\omega_v\right)$)

$$= \frac{\lambda v_p}{4\pi d_m} \frac{1}{M} \int S(\omega_v)\, d\omega_v$$

□

REFERENCES

[1] R. W. Jansen, R. G. Raj, L. Rosenberg, and M. A. Sletten, "Practical multichannel SAR imaging in the maritime environment," *IEEE Trans. Geosci. Remote Sens.*, vol. 56, no. 7, pp. 4025–4036, Jul. 2018.
[2] R. Jansen, M. Sletten, and R. Raj, "Performance studies of emulated multichannel SAR for motion characterization," *IEEE Trans. Aerosp. Electron. Syst.*, vol. 51, no. 4, pp. 3198–3209, Oct. 2015.
[3] M. Sletten, S. Menk, J. Toporkov, R. W. Jansen, and L. Rosenberg, "The NRL multi aperture SAR system," in *Proc. IEEE Radar Conf. (RadarCon)*, Arlington VA, USA, May 2015, pp. 192–197.
[4] R. G. Raj, R. W. Jansen, R. D. Lipps, M. A. Sletten, and L. Rosenberg, "Velocity-ISAR: On the application of ISAR techniques to multichannel SAR imaging," in *Proc. IEEE Radar Conf. (RadarCon)*, May 2015, pp. 1050–1055.
[5] R. W. Jansen, M. A. Sletten, T. L. Ainsworth, and R. G. Raj, "Multichannel synthetic aperture radar based classification of maritime scenes," *IEEE Access*, vol. 8, pp. 127440–127449, 2020.
[6] P. R. Kersten, R. W. Jansen, K. Luc, and T. L. Ainsworth, "Motion analysis in SAR images of unfocused objects using time-frequency methods," *IEEE Geosci. Remote Sens. Lett.*, vol. 4, no. 4, pp. 527–531, Oct. 2007.
[7] J. R. Moreira and W. Keydel, "A new MTI-SAR approach using the reflectivity displacement method," *IEEE Trans. Geosci. Remote Sens.*, vol. 33, no. 5, pp. 1238–1244, Sep. 1995.
[8] P. Leducq, L. Ferro-Famil, and E. Pottier, "Matching-pursuit based analysis of fluctuating scatterers in polarimetric SAR images," in *Proc. IEEE Int. Geosci. Remote Sens. Symp. (IGARSS)*, Sep. 2004, p. 199.
[9] B. Friedlander and B. Porat, "VSAR: A high resolution radar system for ocean imaging," *IEEE Trans. Aerosp. Electron. Syst.*, vol. 34, no. 3, pp. 755–776, Jul. 1998.
[10] J. Li and P. Stoica, "MIMO radar with colocated antennas," *IEEE Signal Process. Mag.*, vol. 24, no. 5, pp. 106–114, Sep. 2007.
[11] A. M. Haimovich, R. S. Blum, and L. J. Cimini, "MIMO radar with widely separated antennas," *IEEE Signal Process. Mag.*, vol. 25, no. 1, pp. 116–129, Jan. 2008.
[12] J. H. G. Ender, P. Berens, A. R. Brenner, L. Rossing, and U. Skupin, "Multi-channel SAR/MTI system development at FGAN: From AER to PAMIR," in *Proc. IEEE Int. Geosci. Remote Sens. Symp.*, vol. 3, Jun. 2002, pp. 1697–1701.
[13] J. Shao, R. Tao, S. Zhou, and Y. Wang, "A novel method of signal processing for VSAR system," in *Proc. Rec. IEEE Int. Radar Conf.*, Alexandria VA, USA, May 2000, pp. 741–744.
[14] R. E. Kell, "On the derivation of bistatic RCS from monostatic measurements," *Proc. IEEE*, vol. 53, no. 8, pp. 983–988, Aug. 1965.
[15] J. Li and P. Stoica, *MIMO Radar Signal Processing*. Hoboken, NJ, USA: Wiley, 2009.
[16] A. Dutt and V. Rokhlin, "Fast Fourier transforms for nonequispaced data," *SIAM J. Sci. Comput.*, vol. 14, no. 6, pp. 1368–1393, Nov. 1993.
[17] S. Bagchi and S. K. Mitra, "The nonuniform discrete Fourier transform and its applications in filter design: Part-1–1-D," *IEEE Trans. Circuits Syst. II, Analog Digit. Signal Process.*, vol. 43, no. 6, pp. 422–433, Jun. 1996.
[18] S. Bagchi and S. K. Mitra, "The nonuniform discrete Fourier transform and its applications in filter design: Part-2–2-D," *IEEE Trans. Circuits Syst. II, Analog Digit. Signal Process.*, vol. 43, no. 6, pp. 434–444, Jun. 1996.
[19] I. G. Cumming and F. H. Wong, *Digital Processing of Synthetic Aperture Radar Data: Algorithms and Implementation*. Norwood, MA, USA: Artech House, 2005.
[20] D. C. Munson, J. D. O'Brien, and W. K. Jenkins, "A tomographic formulation of spotlight-mode synthetic aperture radar," *Proc. IEEE*, vol. 71, no. 8, pp. 917–925, Aug. 1983.

[21] J. V. Toporkov, "A theoretical study of velocity SAR imaging of a moving, nonstationary scene," *IEEE Trans. Geosci. Remote Sens.*, vol. 55., no. 9, pp. 4972–4988, Sep. 2017.
[22] S. J. Frasier and A. J. Camps, "Dual-beam interferometry for ocean surface current vector mapping," *IEEE Trans. Geosci. Remote Sens.*, vol. 39, no. 2, pp. 401–414, Feb. 2001.
[23] O. Christensen, *An Introduction to Frames and Riesz Bases*. Basel, Switzerland: Birkhäuser, 2003.
[24] K. Grochenig, "A discrete theory of irregular sampling," *Linear Algebra Appl.*, vol. 193, pp. 129–150, Nov. 1993.
[25] P. Indyk, M. Kapralov, and E. Price, "(Nearly) sample-optimal sparse Fourier transform," in *Proc. ACM-SIAM Symp. Discrete Algorithms (SODA)*, 2014, pp. 480–499.
[26] S. Heider, S. Kunis, D. Potts, and M. Veit, "A sparse Prony FFT," in *Proc. 10th Int. Conf. Sampling Theory Appl. (SAMPTA)*, 2013, pp. 572–575.

ROBERT W. JANSEN (Member, IEEE) received the Ph.D. degree in theoretical physics from Arizona State University, Phoenix, in 1987. Over more than 30 years of research, he has tackled a broad range of problems in diverse fields, including semiconductor energetics, fluid dynamics, electromagnetic propagation, sonar, and RADAR imaging. In the last 25 years, his efforts have largely been focused in the area of synthetic aperture radar (SAR) and other remote sensing research, mostly as part of the SEALAB section of Code 7260 at the Naval Research Laboratory. He has made numerous significant contributions in areas that include SAR image enhancements, target identification, time-frequency exploitation, and near-shore wave, wind, and surf-zone modeling. He is currently engaged in the development of systems and processing schemes that provide motion measurement and maritime characterization using multi-channel SAR (MSAR) techniques. His awards include Alan Berman Publication Award, Dr. Delores M. Etter Top Scientists and Engineers of the Year Award, and several technology transfer awards.

RAGHU G. RAJ (Senior Member, IEEE) received the Ph.D. degree in electrical engineering from The University of Texas at Austin, in 2007. He is currently a Senior Research Scientist and the Head of the Radar Imaging and Target ID Section, Radar Division, U.S. Naval Research Laboratory (NRL), Washington, DC, USA, where he leads the research and development of advanced methods in statistical signal processing and machine learning with applications to various U.S. DoD funded programs. He has over 70 publications in various international journals, conferences, and technical reports. He holds eight U.S. patents. His research interests include various signal/image processing and machine learning problems in radar and remote sensing. He was a recipient of the NRL Alan Berman Publication Award.